Mechanical properties of lightweight aggregates.

Bernhardt, M., Tellesbø, H., Justnes, H., & Wiik, K.

Correction after revision 1

Mechanical properties of lightweight aggregates

Markus Bernhardt[a], Hilde Tellesbø[b], Harald Justnes[c], Kjell Wiik[a]

[a] Department of Materials Science and Engineering, Norwegian University of Science and Technology, NO-7491 Trondheim, Norway. markus.bernhardt@material.ntnu.no, kjell.wiik@ntnu.no

[b] Weber Leca Rælingen, NO-2008, Fjerdingby, Norway. Hilde.Tellesbo@saint-gobain.com

[c] SINTEF, Building and Infrastructure, NO-7491, Trondheim, Norway. Harald.Justnes@sintef.no

Department of Materials Science and Engineering, Norwegian University of Science and Technology, NO-7491 Trondheim, Norway.

Corresponding author: Kjell Wiik, Department of Materials Science and Engineering, Norwegian University of Science and Technology; Sem Sælands vei 12, 7491 Trondheim, Norway. Email: kjell.wiik@ntnu.no, phone: +4773594082

Abstract

Lightweight aggregates (LWA) were successfully produced both in a pilot-scale rotary kiln and in a laboratory chamber furnace. The mechanical properties of LWA were investigated in detail applying the European standard crushing resistance test (CR-test) as well as the single pellet compression test (spc-test). The spc-test showed that LWA pellets with porosities < 82 % behave similar to solid brittle spheres under compression when considering only the solid fraction of the pellet and the strength may be calculated according to $\sigma_{crit} = F_{crit} / d^2$ where σ_{crit} is a porosity independent strength, F_{crit} is the measured load at failure and d the solid diameter (assuming zero porosity). It was reasoned that catastrophic failure was due to tensile

stresses in the centre of the pellet and the strength was observed to increase exponentially with decreasing sample size. The relationship between the CR- and spc-test has been established facilitating “translation” of strength data between the two different test methods.

Keywords: Lightweight aggregate, mechanical properties, crushing resistance, strength, Weibull modulus

1 Introduction

Artificial lightweight aggregates (LWA) are used in many applications like lightweight concrete, lightweight bricks, as insulation material for road construction or as filter material for water [1-3]. The raw material for LWA can be of different origin, i.e. waste materials like sewage sludge, washing aggregate sludge, waste glass, fly ash etc. or natural raw materials like clay or slate [4-9]. In civil engineering applications like bridges or offshore constructions there is a constant need for lighter and stronger materials, which can be satisfied for instance by lightweight concrete. Various authors showed that the strength of lightweight concrete is influenced by the utilized LWA [10-13], which leads to a certain interest of improving and modifying the mechanical properties of the aggregates. The literature provides several test methods to assess the mechanical strength of LWA. Besides the standard crushing resistance test the most frequently used technique is compression of single LWA pellets. The treatment of the obtained strength data is, however, inconsistent between different studies. Some authors just report the measured load at failure [14-18] others convert the load at failure into a strength (stress) value [4, 19-22] based on an equation derived by Hiramatsu and Oka [23] who investigated the strength of rocks. In order to improve the mechanical properties of LWA

a detailed knowledge on the stress distributions occurring within a spherical pellet during compression is required along with the understanding of factors of importance both to the stress distribution as well as fracture initiation. The aim of the present investigations is to provide this kind of knowledge with a main focus on the influence of porosity and LWA-pellet size on the resulting strength of the pellets. The variation in strength for brittle materials is usually described by the Weibull modulus *m* and the applicability of Weibull theory on strength data obtained for single pellets will be discussed.

2 Material and methods

2.1 Raw materials

The mineralogical and chemical composition of the raw clay was determined by an external research company using gravimetry, wet chemical quantification methods and X-ray diffraction.

2.2 Production of expanded clay aggregates

Lightweight expanded clay aggregates were produced in a pilot scale rotary kiln and manually in the laboratory. The raw material was clay containing 1 % waste oil as expansion agent. Homogenization of the clay as well as the mixing of oil into the clay was performed by shaft mixers in an industrial production line at Saint-Gobain Weber in Norway. The samples produced in the rotary kiln where pre-pelletized in an eirich mixer and fired at about 1120°C in a continuous process with a throughput of approximately 30 kg per hour. The kiln dimensions are 10 m in length and 30 cm of inner diameter. The finished material was

deposited in metal drums and cooled to room temperature. Samples produced in the laboratory were rolled by hand, dried at 105°C, pre-heated for 2 hours at 250°C and finally fired for 8 minutes at 1120°C in a chamber furnace. Just 6-10 pellets where burned at the same time to preserve a constant temperature in the kiln. After the burning process the samples were cooled in air to room temperature.

2.3 Material testing

The material produced in the rotary kiln resulted in pellets with diameters typically ranging between 0.1 mm and 15 mm while pellets produced by hand in the laboratory typically were in the range from 11 mm to 18 mm. Pellets produced in the rotary kiln subjected to investigation were taken from the following fractions (sieved) 1-2 mm, 2-4 mm, 4-6.3 mm, 6.3-8 mm, 8-10 mm and >10 mm.

The average dry particle density, $\rho_{particle}$, of each LWA fraction was determined by sand pycnometry. Between 120 and 4700 pellets (depending on size) were put into a flask and covered with a known amount of fine sand to measure the volume. The particle density was calculated by dividing the mass of the material by the measured volume.

Helium pycnometry was used to determine the density of the solid phase, ρ_{matrix}, consequently denoted as the matrix phase. Each density measurement was performed by planetary milling a couple of pellets to a particle size <36 micron and subsequently assessing the density in an AccuPyc 1330 helium pycnometer from micrometics. The relative density, $\rho_{relative}$, and porosity, *P*, are calculated by Eq. 1 and Eq. 2 respectively.

$$\rho_{relative} = \frac{\rho_{particle}}{\rho_{matrix}} \quad (1)$$

$$P = 100 \cdot \left(1 - \frac{\rho_{particle}}{\rho_{matrix}}\right) \quad (2)$$

Porosity values are given in per cent. The relative density represents a volume ratio between particle and matrix since the mass of gas within a pellet can be neglected compared to the mass of the matrix-phase. The volume of a sphere is proportional to the cube of its radius thus the relative density can be written in the form of Eq. 3.

$$\rho_{relative} = \frac{\rho_{particle}}{\rho_{matrix}} = \frac{(m_{particle} / vol_{particle})}{(m_{matrix} / vol_{matrix})} = \frac{r^3}{R^3} \quad (3)$$

Where *m* is mass, *vol.* volume, *r* the "solid radius" of a sphere with "solid diameter", *d*, and *R* the radius of an expanded pellet with diameter, *D*. The "solid diameter", *d*, is the theoretical diameter of a pellet without any porosity and is calculated by Eq. 4.

$$d = D \cdot \left(\frac{\rho_{particle}}{\rho_{matrix}}\right)^{1/3} \quad (4)$$

The expansion (in %), *E*, of a pellet can be calculated by Eq. 5.

$$E = 100 \cdot \left(\frac{D - d}{d}\right). \quad (5)$$

The crushing resistance of several samples of LWA was determined according to EN 13055-1 [24]. However, in contrast to the description in EN 13055-1 (advising testing of a broad LWA-fraction between 4-22 mm) crushing resistance of narrow fractions of 2-4 mm, 4-6.3 mm, 6.3-8 mm and 8-10 mm of the samples produced in the rotary kiln were investigated.

The loose bulk density (defined in [25]) was determined during the crushing resistance test by measuring the mass of 1 litre of bulk material before it was compacted by vibration.

Single pellet strength was determined by uniaxial compression between 2 parallel rigid platens. The diameter of every aggregate was measured with a calliper before the granule was placed on the bottom plate of a press. Lightweight aggregates usually don't show a perfectly spherical geometry therefore the diameter was measured between the highest and the lowest point when the pellet was lying in a stable position. Compression was performed with a constant speed of displacement of 2 mm per minute until a crack ruptured the sample into at least two larger pieces. The applied load at failure, F_{crit}, was recorded. The test equipment was a press made by instron coupled to a load cell with a maximum capacity of 1 kN. The platen material was alumina. Between 20 and 90 pellets were tested for each sample set depending on the availability of material. The typical quantity was 40-50 pellets to provide a sufficient statistical reliability.

Prior to catastrophic failure, all pellets will suffer a certain "crumbling" (apparent plastic deformation) at the contact point between platens and pellet. The radius, a_c, of this "crumbled area" at the point of failure is important for the calculation of stress distribution (see theory next section) and can be approximated from the average displacement of the piston at breakage, x, and the initial average radius of a sample series, R, by Eq. 6 assuming a perfect sphere and equal damage/crumbling at the top and at the bottom of the pellet.

$$a_c = \left(R^2 - (R - \frac{x}{2})^2 \right)^{\frac{1}{2}} \qquad (6)$$

3 Theory

3.1 Strength testing methods for LWA

Yang and Huang [26] developed a procedure to estimate the strength of LWA by measuring the compressive strength of concrete cylinders containing varying amounts of LWA. This method requires cast lightweight concrete specimens and is therefore inconvenient for a quick strength test of LWA. Another test is reported by Harada et al. [27] who developed the so called "monolayer loading test" to investigate the strength of several pellets at the same time. A couple of pellets are arrayed in one layer and crushed by a piston. This method requires a number of LWA with almost exactly the same size. Inherent to the production process LWA will always exhibit a certain size distribution; additionally the pellets are not completely spherical which makes it more difficult to arrange them in a way that they all have the same height such that the press will crush them all at the same time. EN 13055-1 [24] describes how the crushing resistance of one litre of pellets is determined. The testing procedure is the following: LWA of the sieving fraction 4-22 mm are put into a steel container of one litre volume, compacted by vibration and compressed by 20 mm with a steel piston with a cross section area of 100 cm^2. The total time of the compression process should be approximately 100 seconds. The crushing resistance is calculated by dividing the maximum recorded load by the area of the piston. It has consequently the same dimension as pressure (MPa) and is therefore a potential way to assess the strength of LWA. A disadvantage of EN 13055-1 is that at least 3 litres of compacted bulk material has to be available since the standard is based on three parallels. This method is therefore not applicable to LWA produced in small quantities in a laboratory. Since this is the standard test to determine the mechanical stability of LWA it was incorporated in this study. Another method, which is fast and more appropriate for small quantities, is compression of single pellets between two parallel, rigid

platens. This method is chosen by most researchers when new types of LWA are produced and tested with respect to mechanical strength.

3.2 Strength calculation of brittle spheres under uniaxial compression

One of the main challenges of the single pellet compression test is the calculation of the critical stress that leads to the failure of the particle. A number of different approaches are reported in the literature and Tab. 1 lists a few of the equations developed along with the corresponding material tested. The basic principle is the same, that is, the applied load is related to an area that scales with the size (radius or diameter) of the sample.

Table 1

material / shape	equation	reference
rocks / irregular shape	$\sigma = 0.9F / D^2$	[23, 28]
soil aggregates / irregular shape	$\sigma = 0.576F / D^2$	[29]
soil aggregates, rocks/ irregular shape	$\sigma = F / D^2$	[30-32]
hollow ceramic spheres	$\sigma = F / (\pi R^2)$	[33]

Caption table 1: Equations reported in the literature to determine the stress occurring in a sphere or irregular shaped test piece under uniaxial compression. σ is equal to the stress, F the applied load, D the diameter of the sample and R the radius of the sample.

3.3 Stress distribution and fracture behaviour of brittle spherical particles under uniaxial compression

Hiramatsu and Oka [23] investigated the strength of irregular shaped test pieces to develop a quick method for testing the mechanical properties of rocks. They assumed the stress distribution in a solid, irregular shaped specimen under diametric compression to be the same as in a spherical specimen. The maximum stress is reported to occur along the axis between the two loading points. Li et al. [28] applied the approach of Hiramatsu and Oka [23] successfully to calculate the tensile strength of solid catalysts of spherical shape. By using Weibull statistics [34] Li showed that all the samples revealed the same fracture mode and that failure was due to tensile stresses. Johnson et al. [35] and Chau et al. [36] investigated the fracture behaviour of solid homogeneous spheres made from plaster. Both studies show that spheres under uniaxial compression fracture into hemi-spheres or in up to 6 wedge shaped pieces and 2 cones that occur on the top and on the bottom of the specimen. The formation of the cone shaped pieces is due to Hertzian stresses [37] that occur at the contact area between the platen and the sample [35, 36]. Kschinka et al. [38] observed an explosive like fracture of glass spheres under compression. The whole sample virtually pulverised and no conclusions about fracture mode or crack origin could be deduced from the debris. However, by applying Weibull statistics [34] the authors showed that the fracture origin is most likely to occur within the bulk-phase and not at the surface of the specimen. Similar results were presented by Tsoungui et al. [39] who investigated the size effect on strength and the fracture origin in plaster spheres and cylinders. Shipway and Hutchings [40] presented a numerical solution to calculate the stress distribution within brittle spheres under compression between parallel platens and investigated the fracture of lead glass spheres under the same conditions [41]. The work was based on investigations and calculations of stress distributions in spheres carried out by Dean et al. [42]. The studies show that the maximum tensile stress occurs in the

interior of the sample, as suggested by previous investigators, however, the stress distribution also depends on the ratio between the radius of the contact area between sample and platen, a_c, and the radius of the sample, R. The study shows that for values $a_c / R < 0.6$ the axial tensile stress exceeds the surface tensile stress and given a homogenous flaw distribution throughout the pellet failure will be due to tensile stresses at the centre of the sample rather than at the sample surface.

Investigations on mechanical strength of irregular shaped soil particles were amongst other carried out by McDowell et al. [43-45] and Dexter and Kroesbergen [29]. These studies reviewed again several other works that were assessing the strength of irregular shaped particles. Most studies concluded that the highest tensile stress occurs in the centre of the particle and the strength of the material is given by the load at failure divided by the diameter squared [30, 31] as presented in Tab. 1.

Only a few investigations are related to hollow spheres of macroscopic size. Chung et al. [33] reported hollow brittle spheres to fail due to tensile stresses on the inside of the shell in the region close to contact zone between platen and sample when compressed between two parallel platens. This behaviour was observed experimentally and predicted by computer modelling and later confirmed in another computer simulation by Carlisle et al. [46, 47]. Chung et al. [33] described the hollow spheres to fracture into hemispheres consistent with vertical cracks between the points of contact.

3.4 Fracture, size and the Weibull approach

Strength data of brittle materials is usually described by Weibull statistics [34]. It is based on the weakest link theory and allows a characterization of the reliability of a set of samples [48].

A two-parameter Weibull function in the form of Eq. 7 correlates, the failure probability, F_{prob}, with the applied stress at failure σ_{crit} .

$$F_{prob} = 1 - \exp\left[-\left(\frac{\sigma_{crit}}{\sigma_0} \right)^m \right] \tag{7}$$

Where m is the Weibull modulus describing the reliability or scatter of a sample set and σ_0 a scaling parameter which is referred to as the characteristic stress at which the probability of failure is 0.632. Weibull showed that σ_{crit} is proportional to the $-(1/m)$ power of its volume. The Weibull modulus m can also be interpreted as the density of Griffith flaws [49] within the tested volume.

The force, F_{crit} , needed to crush a brittle spherical particle increases with the particle diameter, D, following a power law in the form [39, 50, 51]

$$F_{crit} = kD^{\alpha} \tag{8}$$

Where k is an empirical constant, the exponent α is given for a volume fracture mode by Eq. 9

$$\alpha = \frac{2m-3}{m} \tag{9}$$

and in the case of contact fracture by Eq. 10 [39].

$$\alpha = \frac{2m-3}{m+3} \tag{10}$$

Consequently, if one determines the exponent α in Eq. 8 and the fracture mechanism is known it is possible to calculate the Weibull modulus. Eq. 11 and Eq. 12 are derived from Eq. 9 and Eq. 10 to calculate *m* in case of volume fracture and contact fracture respectively.

$$m = \frac{-3}{\alpha - 2} \tag{11}$$

$$m = \frac{3\alpha + 3}{2 - \alpha} \tag{12}$$

4 Results

Tab. 2 shows the mineralogical and chemical composition of the raw clay. The data is presented as received and was not normalized to 100 %. Tab. 3 presents an overview of the properties of the expanded clay aggregates produced in the rotary kiln (denoted as "rot- average sample diameter rounded") and in the laboratory (denoted as "lab- average sample diameter rounded"). The diameter and the load at failure were determined for every single pellet and are given as the average of all tested samples (± the standard deviation) whereas the other values (d, $\rho_{particle}$, P, $\rho_{relative}$) are based on a number of simultaneously tested pellets.

Table 2

mineralogy	content	chemistry	content
Quartz	17	SiO_2	59
Plagioclase	19	Al_2O_3	18
Orthoclase	6	Fe_2O_3	7
Amphibole	4	K_2O	4
Ilite/muscovite	40	MgO	3
Chlorite	10	CaO	2
Fe-Oxihydate	4	Na_2O	1

	TiO_2	1
	$LOI_{(1000°C)}$	5

Caption Table 2: Approximate mineralogical and chemical composition of the raw clay; Results are presented in wt.-%.

Table 3

sample	average diameter, D [mm]	sieving fraction [mm]	solid diameter, d [mm]	particle density, $\rho_{particle}$ [g/cm^3]	porosity, P [%]	relative density, $\rho_{relative}$	load at failure, F_{crit} [N]	numbe of teste sample
rot-2	1.9 (±0.12)	1-2	1.2	0.67	75	0.25	14 (±5)	50
rot-4	3.6 (±0.29)	2-4	2.2	0.58	78	0.22	34 (±8)	50
rot-5	5.3 (±0.72)	4-6.3	3.1	0.53	80	0.20	57 (±17)	50
rot-7	7.1 (±0.48)	6.3-8	4.0	0.49	82	0.18	83 (±24)	50
rot-9	8.8 (±0.66)	8-10	4.9	0.46	83	0.17	101 (±26)	90
rot-12	11.7 (±0.77)	> 10	6.1	0.39	86	0.14	121 (±45)	50
lab-11	11.4 (±0.26)	-	6.4	0.49	82	0.18	86 (±19)	43
lab-13	12.8 (±0.44)	-	7.3	0.50	82	0.18	101 (±19)	22
lab-14	13.8 (±0.56)	-	7.8	0.49	82	0.18	118 (±22)	40
lab-15	15.3 (±0.59)	-	8.4	0.45	83	0.17	116 (±33)	21
lab-16	16.0 (±0.55)	-	8.8	0.46	83	0.17	116 (±29)	72
lab-17	17.3 (±0.63)	-	9.4	0.43	84	0.16	110 (±28)	39

Caption Table 3: Overview of the properties of samples produced in the rotary kiln (rot-) and in the laboratory (lab-); the numbers denote average diameter rounded in mm. Standard deviations are given in brackets.

4.1 Material description

Fig. 1 pictures a representative pellet of each fraction of the material produced in the rotary kiln. The pellets exhibit an almost spherical shape and a relatively homogeneous outer shell

which is the result of the constant rotation of the samples during the burning process. Fig. 2 shows representative pellets of each fraction produced in the laboratory. Due to the differences in production (no rotation) the shape is somehow less spherical compared to samples from the rotary kiln and the outer shell is more heterogeneous and can be divided in two different types. One type is thick and dense and originates from the aggregate surface prior to expansion, the other type is a more porous surface formed during the expansion process. Fig. 3 displays a typical example of such a specimen with the dense shell in the lower hemisphere and the more porous shell in the upper hemisphere. The general internal structure is fairly similar throughout all samples. Each specimen consists of the typical features of LWA which are a highly porous core containing a rather broad distribution of pore size and shape and a denser outer shell. Fig. 4 shows these features for one specimens of the series rot-5. The interface between the shell and the bulk-phase (the term bulk-phase consequently denotes the porous interior of one pellet) is in most cases not well defined, hence a reliable value for the typical shell thickness of a series of pellets could not be determined.

Figure 1

Caption Fig. 1: Illustration of LWA pellets produced in a pilot-scale rotary kiln. Diameters range from 1.8 mm (left) up to 12 mm (right).

Figure 2

Caption Fig. 2: Illustration of LWA pellets produced in a chamber furnace in the laboratory. Diameters range from 11 mm (left) up to 17 mm (right).

Figure 3

Caption Fig. 3: Illustration of one pellet of the series lab-16 (16 mm diameter) picturing the heterogeneity of the outer shell. The lower hemisphere exhibits a dense shell; the upper hemisphere exhibits a more porous shell.

Figure 4

Caption Fig. 4: Light microscope picture of the cross-section of a LWA pellet of 6 mm diameter produced in the rotary kiln showing the typical features of an LWA: A highly porous core surrounded by a relatively dense thin shell. The total porosity of the displayed pellet is approximately 82 %.

4.2 Material properties

The change of particle density, $\rho_{particle}$, and porosity, *P*, with the particle diameter, *D*, is given in Fig. 5 for all samples. The rotary kiln samples show a clear trend of decreasing particle density and increasing porosity with increasing diameter. Hence, the bigger the pellet the more it expanded during the firing process leading to a lower density. Fig. 6 visualizes the expansion in per cent, *E*, (the "bloating index" [20, 52] utilized in other studies describes basically the same phenomena) in dependency of the pellet diameter, *D*. And Fig. 7 shows the pellet diameter, *D*, as a function of the size of the unburned pellet denoted as "solid diameter", *d* (calculated with the assumption *P*=0). Fig. 6 and Fig. 7 imply that the final pellet diameter, *D*, is a function of the size (and consequently mass) of the unburned pellet, *d*, and the expansion, *E*, and additionally, the expansion is proportional to the size of the unburned pellet.

The material produced in the laboratory shows generally the same trends as the rotary kiln samples however less dependent on the pellet diameter, *D*, and solid diameter, *d*.

The density of the matrix phase ranges from 2.61 g/cm^3 to 2.73 g/cm^3 without any systematic correlations to other properties. This value is generally governed by the raw material and the heat treatment during the production process. Since both variables are quite constant throughout the same production process, the small variations in the matrix density can be

explained by the heterogenic nature of the material. Fig. 5 illustrates the close correlation between particle density, $\rho_{particle}$, and porosity, P, throughout all sample series and hence shows the general consistency of the matrix density for different sized pellets of the same production process.

Figure 5

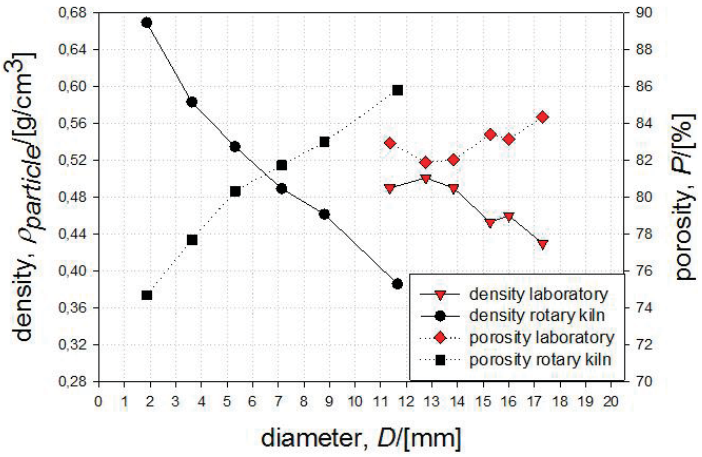

Caption Fig. 5: Particle density, $\rho_{particle}$, and porosity, P, of all samples produced in the rotary kiln and in the laboratory.

Figure 6

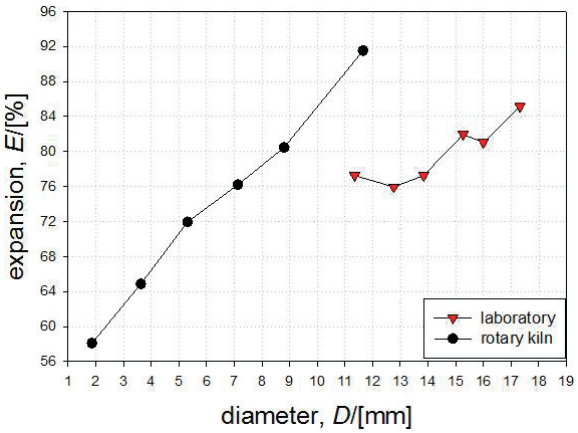

Caption Fig. 6: Calculated, theoretical expansion, E, of all samples.

Figure 7

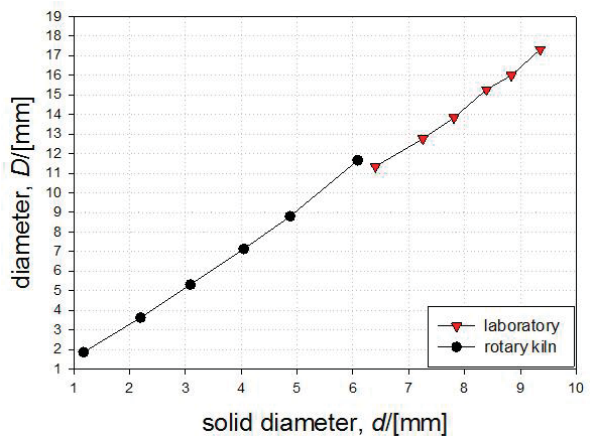

Caption Fig. 7: Final sample diameter, *D*, as function of the solid diameter, *d*.

4.3 Single pellet compression

Results of the single pellet compression test are presented in Fig. 8. The experimentally determined value for the average load at failure, F_{crit}, of the sample is plotted in dependency of the pellet diameter, *D*. The error bars represent the standard deviation of the sample sets showing a significant scatter in F_{crit}. A better overview of the extent of the scatter of the load at failure and the diameter within a sample series is given in Fig. 9. The relative standard deviation (standard deviation in per cent of the average value) of the load at failure, F_{crit}, and the diameter, *D*, are displayed. The relative standard deviation of F_{crit} of the rotary kiln samples varies between 22 % and 40 % with an average of 30 %. In case of the laboratory samples the average value of the variation is 23 %. The average diameter, *D*, of a sample series produced in the rotary kiln exhibits a relative standard deviation of 7 %. Rot-5 (fraction 4-6.3 mm, ct. Tab. 3) shows an increased value of 14 % which is due to the large size range of 2.3 mm compared to the other fractions that show a maximal size range of 2 mm (Tab. 3).

Samples produced in the laboratory exhibit a size variation of around 4 % in average. In the succeeding graphs error bars are omitted for sake of clarity. Additionally, it is not possible to determine the standard variation for all properties since some of them (i.e. density or porosity) are calculated from the average values of several pellets and not from each single specimen within a series. Generally there is a large scatter in properties due to the heterogeneous nature of the material, therefore a large amount of samples were normally tested to obtain a representative average value.

Figure 8

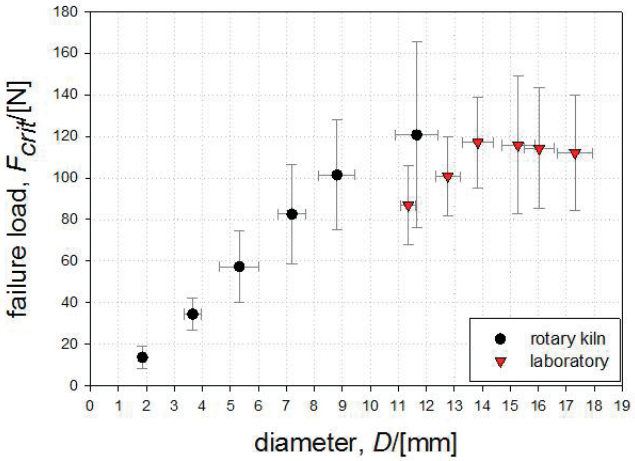

Caption Fig. 8: Failure load for all sample series; determined by the spc-test; error bars represent the standard deviation.

Figure 9

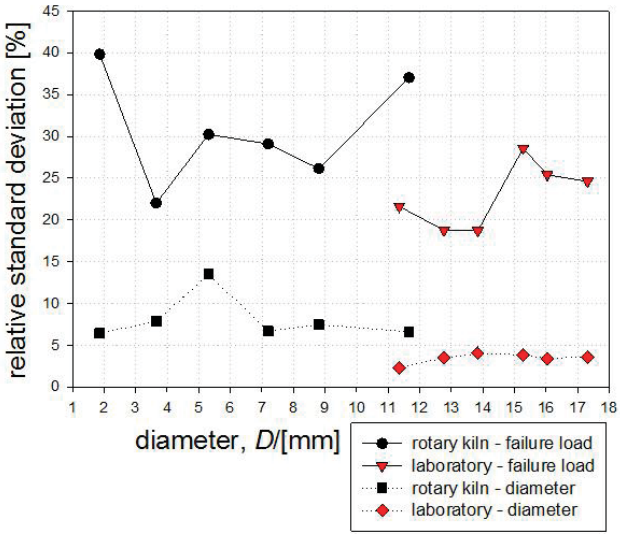

Caption Fig. 9: Relative standard deviation (%) of the failure load, F_{crit}, and the pellet diameter, *D*.

4.4 Fracture of lightweight aggregates under uniaxial loading conditions

When a single LWA pellet is compressed between two rigid platens the top and bottom of the aggregate get crumbled before the sample ruptures into two to four pieces. The fracture behaviour can be described as quasi elastic, meaning that the sample gets deformed by crumbling before a brittle fracture (catastrophic failure) occurs. Fig. 10 shows a typical load-displacement graph of the compression of a LWA pellet with a constant speed of displacement of 2 mm/min. “Local minima” in the applied load occur, basically due to the above described crumbling, however there is a linear trend until catastrophic failure. Fig. 11 a) shows a ruptured LWA pellet. In this case the sample splits into 3 fragments and the porous interior is clearly seen due to the crumbling effect. Fig. 11 b)-c) show typical fracture patterns where the sample is split into two and four pieces respectively. It should be mentioned that

the samples produced in the laboratory generally tend to break rather into two hemispheres whereas the samples produced in the rotary kiln randomly split in two to four pieces.

Figure 10

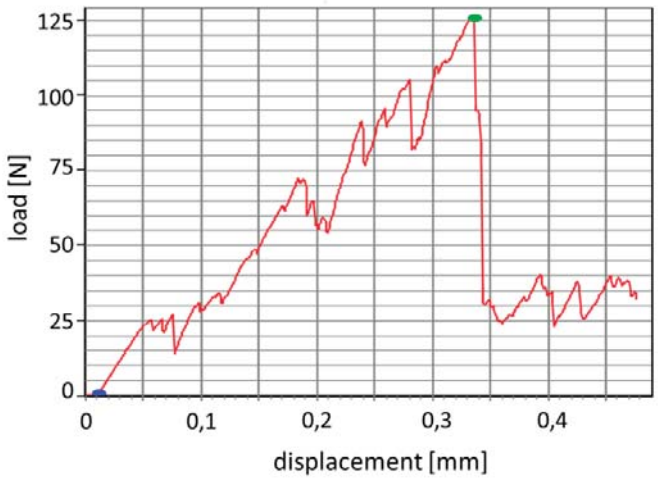

Caption Fig. 10: Typical load- displacement graph resulting from the compression of a single LWA pellet between rigid, parallel platens with a constant speed of displacement, 2 mm/min (spc-test).

Figure 11 a-c

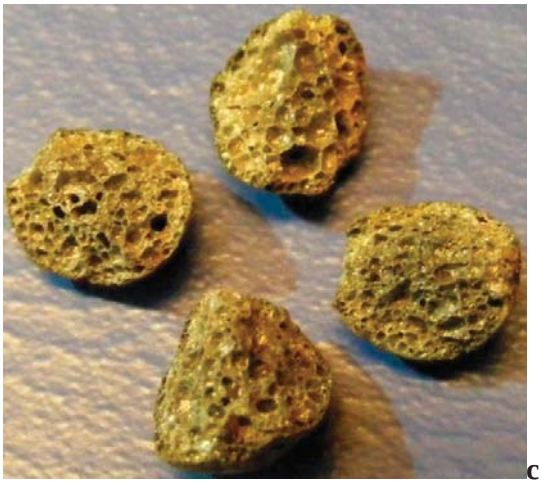

Caption Fig. 11: Fracture patterns of LWA pellets after the spc-test. a) ruptured LWA pellet; b) typical fracture pattern of a pellet that splits into two hemispheres; c) typical fracture pattern of a pellet that splits into four evenly shaped pieces.

4.5 Crushing resistance (EN 13055-1)

The crushing resistance, *C*, was determined for the samples rot-4, rot-5, rot-7 and rot-9. All the remaining samples were not available in sufficient amount to perform this type of investigation. The results are presented in Fig. 12 including the loos bulk density of the tested samples. The crushing resistance increases with both, decreasing sample diameter, *D*, and increasing bulk density.

Figure 12

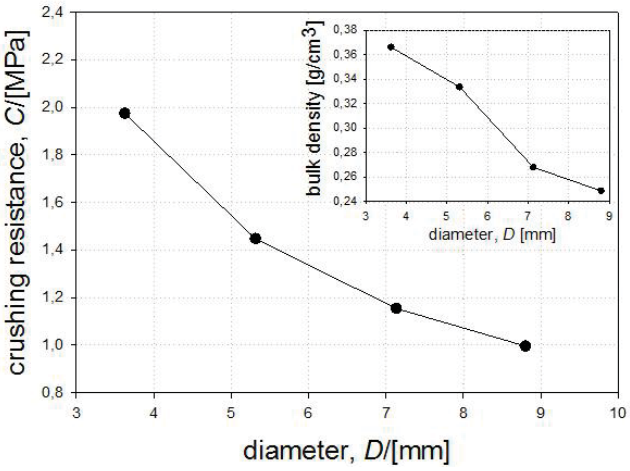

Caption Fig. 12: Crushing resistance, *C*, determined according to EN 13055-1 for the rot-4 to rot-9 samples; the insertion shows the loose bulk density for the same samples.

5 Discussion

5.1 Prediction of the load at failure for single pellet compression

Various equations have been proposed (Tab. 1) to describe the stress distribution and strength of brittle spheres. In order to apply one of these equations to lightweight aggregates the general fracture behaviour of LWA has to be similar to the fracture behaviour of the material these equations were developed for. The described fracture pattern of LWA (section 4.4) is similar to observations made during compression tests of solid, brittle spheres [35, 36, 39] which is an indication that failure is caused by similar stresses within the bulk-phase of the pellet. However, due to the core-shell structure and the high porosity levels of LWA it is not automatically given that the stress is distributed in the same way as in solid, brittle spheres when being compressed. Since the stress distribution in the material cannot be directly

measured a correlation between the load at failure, F_{crit}, and another measurable macroscopic property of importance to the stress distribution needs to be found. It is assumed that these properties may be divided into two general groups: The first one is the strength of the matrix material which is influenced by the mineralogical composition, the amount of glass phase and the density of micro cracks which again is influenced by the thermal history of the material and its composition. The second group includes geometrical factors of the pellet as a whole which are the diameter, total porosity, pore size distribution, shape of the pellet, thickness of the shell, material distribution in core and shell etc. Additionally the shape of a pellet is not constant but changes during the test as it gets crumbled at the point of contacts between pellet and platens. All these variables may play a role and more or less affect the value of F_{crit}.

In the case of solid, brittle spheres it has been reported that the load at failure increases with the sphere diameter following a power law [39, 50, 51] when the specimens are compressed between parallel platens. Fig. 13 displays the development of the load at failure, F_{crit} , determined by single pellet compression with the size of LWA pellets on a log-log-scale. The sample size is represented in the form of the actual diameter, *D*, and as the solid diameter, *d*, calculated by Eq. 4. Just considering the 4 smallest sample series of the rotary kiln (rot-2 to rot-7) and the 3 smallest sample series of the laboratory samples (lab-11 to lab-14) a linear trend is observed independent of the type of diameter applied (*d* or *D*). The solid and dashed lines in Fig. 13 are the linear regressions of the samples described above for both *d* and *D*. The slopes are 1.46 (for *d*) and 1.34 (for *D*) for the rotary kiln samples and 1.56 (for *d*) and 1.58 (for *D*) for the laboratory samples. Values reported in the literature range from 1.5 for cement grains [51], 1.6 for plaster spheres [39] and 1.44 for glass spheres [50]. Consequently, when taking the solid diameter into consideration samples of both production processes are in the range of solid brittle spheres. Hence, for the smaller fractions of LWA the load at failure is correlated with the solid diameter in the same way as observed for solid, brittle spheres.

However, as the sample size increases deviation from linearity is evident for both types of production processes (applying for the samples: rot-9, rot-12 and lab-15 to lab-17). Fig. 14 shows the load at failure, F_{crit}, in terms of d on a lin-lin-scale and porosity values, P, are added as numbers. The solid lines are derived from the regressions given in Fig. 13 and correspond to Eq. 13 for the rotary kiln samples and Eq. 14 for the laboratory samples.

F_{cal} represents the calculated load at failure and d the solid diameter of the sample. Both equations are given in the form of Eq. 8.

$$F_{cal} = 10.83 \cdot d^{1,46} \tag{13}$$

$$F_{cal} = 4.68 \cdot d^{1,56} \tag{14}$$

These functions predict the result of the single pellet crushing test for a given solid diameter, d, with the following limitation: Once the porosity exceeds 82 % the measured load at failure deviates from the theoretically predicted trend towards lower values. This effect is observed independently from both the production process and the absolute sample size. The deviation from the predicted strength may be due to thinner, less stable solid walls within the bulk-phase and/or by a decrease in the total amount of connected solid walls.

It can be noted that for a given production process the load at failure of LWA is basically dependent on the particle size and the total porosity. Most of the other mentioned properties that might influence F_{crit} are constant for a given production process or seem to have a minor impact on the measured value. In case the porosity does not exceed a certain threshold of about 82 % the load at failure can be predicted with Eq. 13 and Eq. 14.

Figure 13

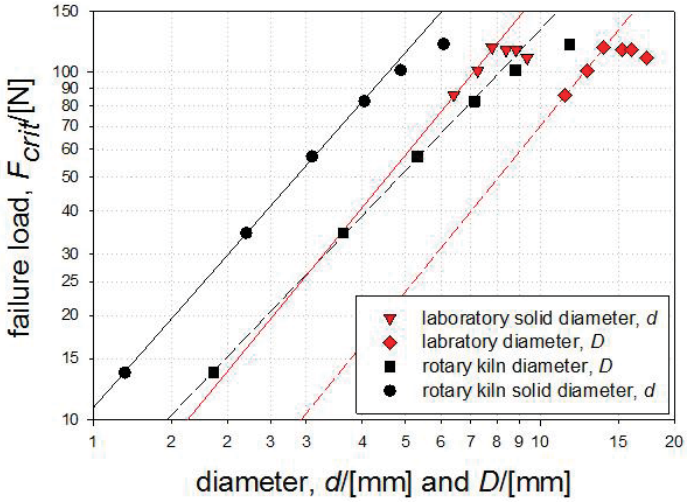

Caption Fig. 13: Failure load, F_{crit}, in dependency of the solid diameter, d, and the actual diameter, D, for all samples. The solid and dashed lines are the linear regressions of the series rot-2 to rot-6 and lab-11 to lab-14 respectively.

Figure 14

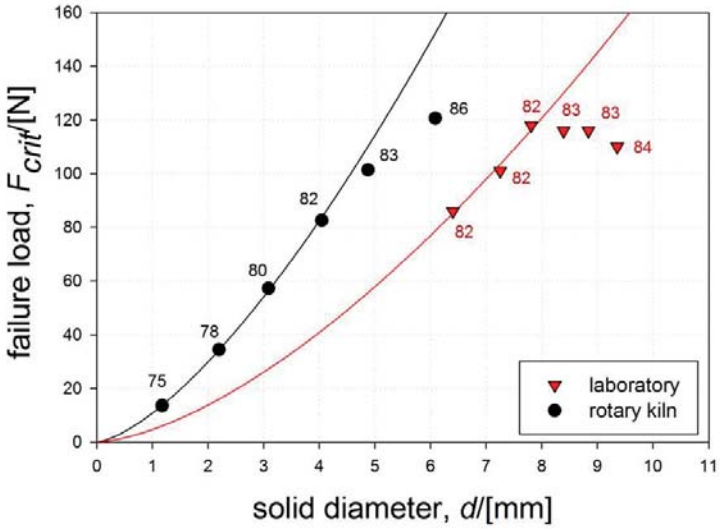

Caption Fig. 14: Failure load, F_{crit}, in dependency of the solid diameter, d, for all samples. The numbers denote the total porosity, *P (%)*. Eqs. 13-14 are represented by the solid lines.

5.2 Fracture origin and calculated strength for LWA pellets with porosities P < 82 %.

It has been shown that LWA with porosities up to 82 % behave similar to solid brittle spheres under compression when taking the solid fraction of the pellet into consideration (Fig. 13-14). Hence, it is reasonable to consider whether one of the equations given in Tab. 1 is able to convert the measured load at failure, F_{crit}, into a strength (stress) value, σ_{crit}. These equations just differ in the pre-factor and it is suggested to utilize the simplest approach with a pre-factor of 1 as done for instance by [30-32, 43-45]. The resulting equation can be written as

$$\sigma_{crit} = \frac{F_{crit}}{d^2} \tag{15}$$

Where σ_{crit} is the stress leading to failure, F_{crit} the load at failure and d the solid diameter of the LWA pellet. Eq. 15 describes a porosity independent strength value for LWA. According to [23, 28, 38, 39] solid spheres basically fail due to tensile stresses within the bulk-phase of the specimen when compressed between parallel platens. Since the LWA pellets also behave similar to solid, brittle spheres with respect to fracture (Fig. 13) it is likely that LWA pellets also fail due to tensile stresses within the bulk-phase. Consequently σ_{crit} in Eq. 15 can the seen as the tensile strength of LWA and will be denoted as solid strength referring to the dependency on the solid amount of material in the pellet.

It was reported in chapter 3.3 that the stress distribution within a spherical particle will be influenced by the ratio between the radius of the contact area between platen and sample, a_c, and the radius of the sample, R. In case of LWA the radius of the contact area, a_c, can be estimated by Eq. 6 from the crushed part at the top and at the bottom of the sample (ct. Fig. 11a). The measured load at failure might give a false impression of the actual occurring

tensile stresses within the pellet in case a_c is relatively large compared to the radius of the sample, R [40, 41]. Additionally, when comparing different samples the ratio a_c / R should be similar to ensure that the load at failure reflects the same stresses in all samples. Ratios a_c / R for LWA were found to range from 0.35 to 0.43 for the rotary kiln samples and from 0.24 to 0.29 for samples produced in the laboratory. According to Shipway and Hutchings [40, 41] the tensile stress along the load axis does not change significantly for $0.2 < a_c / R < 0.6$ and the axial tensile stress always exceeds the surface tensile stress. This emphasizes that LWA most likely fail due to tensile stresses at the given loading conditions.

5.3 Fracture origin and calculated strength for LWA with porosities P >82 %

Once LWA pellets exceed a porosity of approximately 82 % the mechanical behaviour deviates from the predicted behaviour as discussed in section *5.1*. One possible explanation is that the stress distribution changes significantly at some threshold value of the porosity, $P_{threshold}$, corresponding to a change in fracture mechanism and therefore deviating from the predicted load at failure, F_{crit}. Well above $P_{threshold}$ the LWA pellets may behave similar to hollow spheres and fail as described by Chung [33] due to tensile stresses on the inside of the shell in the region close to contact zone between platen and sample. However, no final evidence supporting such significant change in fracture behaviour could be found. On the other side, a possible change in fracture mechanism for highly porous bodies was reported by Miyoshi et al. [53]. They observed a significant decrease in tensile yield strength in aluminium foams as a certain porosity threshold (about 80 %) was exceeded. The underlying reasons were explained as changes in pore morphology. Though the type of failure is quite different for Al-foams (ductile) compared with LWA (brittle), it is interesting to notice that there is a shift in mechanism at very high porosities for both type of materials. To finally

clarify the mechanisms governing the decrease in strength at high porosities further investigations will be necessary.

5.4 Strength comparison between LWA produced in the laboratory and LWA produced in the rotary kiln

The development of the solid strength of LWA with the solid diameter is displayed in Fig. 15 for samples produced in the laboratory and in the rotary kiln. The solid lines represent the trends of pellets with porosities lower than 82 % and the circles and triangles represent the experimental data. All values were calculated by Eq. 15. Samples deviating from the trend line represent porosities above 82 %. The strength of the LWA pellets generally increases with decreasing solid diameter consistent with the inherent properties of brittle materials: With decreasing sample volume the probability of finding a critical flaw that leads to failure for a given stress decreases. Fig. 15 enables a comparison between the two different production processes. The samples produced in the laboratory show a lower strength than the samples produced in the rotary kiln. A possible explanation is the difference in cooling rates that the pellets experience after expansion. The samples from the rotary kiln were produced in large amounts and directly transferred to metal drums for storage, hence subjected to a relative slow cooling rate due to the low thermal conductivity of this highly porous material. However, the batches produced in the laboratory were typically only a few pellets and after expansion they were taken directly out of the furnace and cooled at ambient temperature, hence these pellets were virtually exposed to a thermal shock which potentially initiate micro cracks and subsequent less mechanical strength.

Figure 15

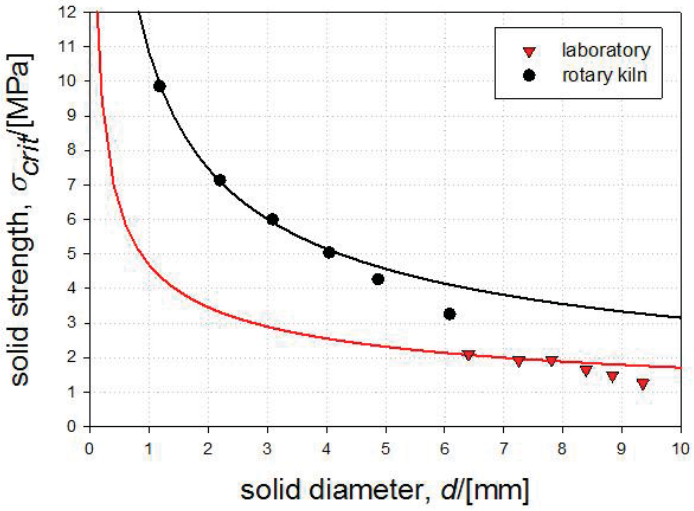

Caption Fig. 15: Solid strength, σ_{crit}, as a function of the solid diameter, d, for all samples.

The solid lines represent the trend of pellets with porosities less than 82 %. Pellets with porosities >82% show less strength than predicted by the solid lines.

5.5 Determination of the Weibull modulus m of LWA

The Weibull modulus m is a measure of the reliability of brittle materials and thus an interesting parameter for LWA. Usually this value is determined by establishing Weibull-plots where the failure probability of several samples is plotted against the stress at failure on a double logarithmic scale. The m value results from the slope of the regression of that graph. This method is not applicable due to the fact that the actual stress that leads to failure of every single pellet is unknown. The stress generated in a pellet is calculated by Eq. 15 which also includes the porosity of the pellet. The porosity was not determined for every single pellet but just for the respective sample series. Taking the average porosity of a sample series into account to predict the strength of each single specimen induces a large error in the calculation

and hence would give an incorrect value for *m*. An approximation of the *m* value of LWA is anyway possible with the method described in section *3.4*. In section *5.2* arguments were given supporting the assumption that volume fracture is the most probable fracture mode for lightweight aggregates. Hence, the Weibull modulus can be calculated by Eq. 11 when considering just the samples that show the same behaviour as solid brittle spheres under compression. With the exponent α in Eq. 13 and Eq.14 a Weibull modulus of 6.82 for samples produced in the laboratory and 5.55 for sample produced in the rotary kiln was determined. These values are in good agreement with data reported in the literature for similar materials like porous phosphate glass ceramics [54] or glass spheres [38]. The variation in *m* results from the differences in the production process.

5.6 Relation between solid strength and crushing resistance

The results of the crushing resistance test can be approximated from the solid strength values determined by single pellet compression with the following equations (the underlying calculations and assumptions are presented in the appendix).

$$C \approx \frac{F_{crit}}{D^2} \cdot \left(\frac{\rho_{bulk}}{\rho_{particle}} \right)^{\frac{2}{3}} \tag{16}$$

$$C \approx \frac{F_{crit}}{D^2} \cdot 0,74 \tag{17}$$

Where C is the crushing resistance, F_{crit} the load at failure recorded by singe pellet compression and D the actual diameter of the pellet. Eq. 16 takes the actual packing density of aggregates within the steel container of the crushing resistance test into consideration

whereas Eq. 17 approximates the packing density from a literature value of 0.64 [55] for the highest random packing density of equally sized spheres. The results of the calculated crushing resistance using Eq. 16 and Eq. 17 are presented in Fig. 16 in comparison to the measured crushing resistance. The “calculated crushing resistance 1” is the result of Eq. 16 and the “calculated crushing resistance 2” is the result of Eq. 17. Both solutions correspond well with the measured crushing resistance. However the values of the “calculated crushing resistance 2” give a better fit with the measured data than the “calculated crushing resistance 1”. To solve Eq. 16 the loose bulk density was taken into consideration but the bulk material was compacted by vibration before the crushing resistance test was performed and the actual (compacted) bulk density at the moment of crushing was not determined and will be slightly higher than the loos bulk density. This might be the reason why the theoretical packing density (used in Eq. 17) leads to better results than the measured packing density (used in Eq. 16). It should be pointed out that it is not necessary to know the bulk density of the material to elaborate the crushing resistance by Eq. 17 thus the “calculated crushing resistance 2“ is given for all sample series produced in the rotary kiln.

Eq. 16 and Eq. 17 enables us to convert the solid strength into the crushing resistance and vice versa. That implies that Eq. 15 describes the strength of porous, almost spherical particles quite well. Eq. 17 can be utilized to relate crushing resistance and solid strength in case the investigated particles are almost of the same size whereas Eq. 16 should also be applicable to broader size fractions.

Figure 16

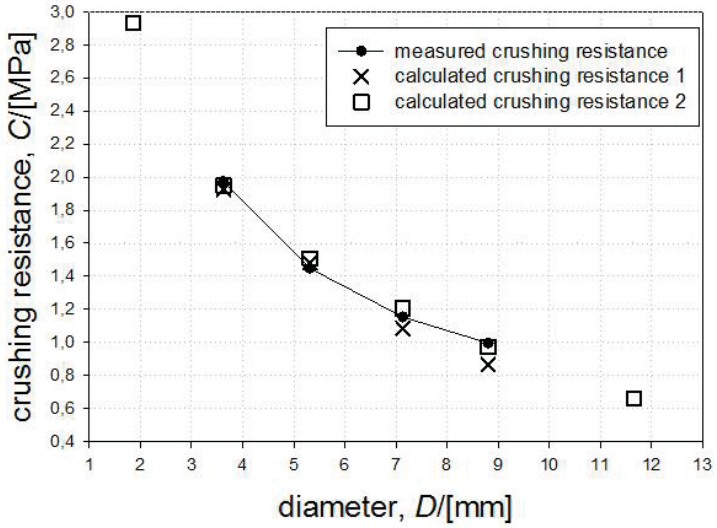

Caption Fig. 16: Correlation between measured crushing resistance and calculated crushing resistance. The calculated crushing resistance 1 and 2 are based on Eqs. 16-17.

6. Conclusions

Lightweight expanded clay aggregates of varying size and porosity were successfully produced both in a pilot-scale rotary kiln and in a chamber furnace in the laboratory. The pellets were investigated with respect to mechanical properties applying the method of the European standard crushing test (CR-test) as well as the single pellet compression test (spc-test) on more than 550 samples

The spc-test showed that LWA pellets with porosities <82 % behave similar to solid brittle spheres under compression when considering only the solid fraction of the pellet and the strength may be calculated according to $\sigma_{crit} = F_{crit} / d^2$ where σ_{crit} is a porosity

independent solid strength, F_{crit} is the measured load at failure and d the solid diameter (assuming zero porosity). It was reasoned that catastrophic failure was due to tensile stresses in the centre of the pellet and the strength was observed to increase exponentially with decreasing sample size. However, deviation (lower strength) from exponential behaviour was observed at porosities typically >82%.

A reasonable approximation for the assessment of the Weibull modulus (*m*) for LWA has been identified and *m* was found to vary between 5.5 for rotary kiln samples and 6.8 for laboratory samples.

The relationship between the CR- and spc-test has been established, facilitating "translation" of strength data between the two different test methods. This may represent a new and useful tool applicable also on an industrial scale related to quality monitoring and assessment.

Appendix:

Calculations to describe the relation between solid strength and crushing resistance

It is assumed that the result of the crushing resistance test is dependent on the volume ratio of solid material and the strength of the solid material within the test cylinder. Assuming that the fracture mechanism is the same for single pellet compression and crushing resistance the following correlation between solid strength of single pellets and crushing resistance can be postulated:

$$C \cdot \frac{1}{(\rho_{relative(c)})^{2/3}} \approx \sigma_{crit} \qquad (18)$$

Where C is the crushing resistance, the solid strength, σ_{crit}, is calculated by Eq. 15 and $\rho_{relative(c)}$ represents the volume ratio between bulk material and matrix material within the cylinder and is calculated in the same way as the relative density, $\rho_{relative}$, in Eq. 1:

$$\rho_{relative(c)} = \frac{\rho_{bulk}}{\rho_{matrix}} \tag{19}$$

Where ρ_{bulk} is the bulk density and ρ_{matrix} is the matrix density. Eq. 18 normalizes the area of the piston of the crushing resistance test by the ratio of solid material theoretically found in a random plane trough the test cylinder following the same idea as for the calculation of the solid strength, σ_{crit}, of single pellets. Considering Eq. 3, 4 and 15 and neglecting the contribution of gas trapped within a pellet to the total mass of a pellet, Eq. 18 can be formulated in the following way:

$$C \approx \frac{F_{crit}}{D^2} \cdot \left(\frac{\rho_{matrix}}{\rho_{particle}} \right)^{\frac{2}{3}} \cdot \left(\frac{\rho_{bulk}}{\rho_{matrix}} \right)^{\frac{2}{3}} \tag{20}$$

Eq. 20 can be simplified in the form

$$C \approx \frac{F_{crit}}{D^2} \cdot \left(\frac{\rho_{bulk}}{\rho_{particle}} \right)^{\frac{2}{3}} \tag{16}$$

The density ratio in Eq. 16 equals the packing density of the bulk material in the steel container of the crushing resistance test. Assuming closest random packing of equally sized particles of 0.64 [55] Eq. 16 can be written in the from:

$$C \approx \frac{F_{crit}}{D^2} \cdot 0.74 \qquad (17)$$

Acknowledgements

The financially support of Saint-Gobain-Weber and COIN (concrete innovation center) as a part of SINTEF is gratefully acknowledged

Glossary

LWA	lightweight aggregate
CR-test	crushing resistance test
spc-test	single pellet compression test
$\rho_{particle}$	particle density
ρ_{matrix}	matrix density
ρ_{bulk}	bulk density
$\rho_{relatice}$	relative density
P	porosity
m	mass
r	solid radius (zero porosity)
d	solid diameter (zero porosity)
R	radius
D	diameter
E	expansion
F_{crit}	load at failure
a_c	radius of the crushed area on top and bottom of the pellet / contact area between sample and platen

x	absolute displacement of the piston
F_{prob}	failure probability
σ_{crit}	stress at failure / solid strength
m	Weibull modulus
σ_0	scaling parameter (failure probability 0.632)
k	empirical constant
C	crushing resistance

References

1. Nkansah, M.A., et al., The use of lightweight expanded clay aggregate (LECA) as sorbent for PAHs removal from water. Journal of Hazardous Materials, 2012. 217-218: p. 360-365.
2. Øiseth, E. and G. Refsdal. Lightweight aggregates as frost insulation in roads - Design chart. 2007. Orono, ME.
3. Ausland, G., et al., Intermittent filtration of wastewater - Removal of fecal coliforms and fecal streptococci. Water Research, 2002. 36(14): p. 3507-3516.
4. Cheeseman, C.R. and G.S. Virdi, Properties and microstructure of lightweight aggregate produced from sintered sewage sludge ash. Resources, Conservation and Recycling, 2005. 45(1): p. 18-30.
5. González-Corrochano, B., et al., Microstructure and mineralogy of lightweight aggregates produced from washing aggregate sludge, fly ash and used motor oil. Cement and Concrete Composites, 2010. 32(9): p. 694-707.

6. Ducman, V., A. Mladenovič, and J.S. Šuput, Lightweight aggregate based on waste glass and its alkali-silica reactivity. Cement and Concrete Research, 2002. 32(2): p. 223-226.

7. Huang, S.C., et al., Production of lightweight aggregates from mining residues, heavy metal sludge, and incinerator fly ash. Journal of Hazardous Materials, 2007. 144(1-2): p. 52-58.

8. Swamy, R.N. and G.H. Lambert, The microstructure of Lytag aggregate. International Journal of Cement Composites and Lightweight Concrete, 1981. 3(4): p. 273-282.

9. Arioz, O., et al., A preliminary research on the properties of lightweight expanded clay aggregate. Journal of the Australian Ceramic Society, 2008. 44(1): p. 23-30.

10. Lo, T.Y., W.C. Tang, and H.Z. Cui, The effects of aggregate properties on lightweight concrete. Building and Environment, 2007. 42(8): p. 3025-3029.

11. Cui, H.Z., et al., Effect of lightweight aggregates on the mechanical properties and brittleness of lightweight aggregate concrete. Construction and Building Materials, 2012. 35: p. 149-158.

12. Swamy, R.N. and G.H. Lambert, Mix design and properties of concrete made from PFA coarse aggregates and sand. International Journal of Cement Composites and Lightweight Concrete, 1983. 5(4): p. 263-275.

13. Ke, Y., et al., Influence of volume fraction and characteristics of lightweight aggregates on the mechanical properties of concrete. Construction and Building Materials, 2009. 23(8): p. 2821-2828.

14. Hwang, C.L., et al., Manufacture and performance of lightweight aggregate from municipal solid waste incinerator fly ash and reservoir sediment for self-consolidating lightweight concrete. Cement and Concrete Composites, 2012. 34(10): p. 1159-1166.

15. Bui, L.A.T., et al., Manufacture and performance of cold bonded lightweight aggregate using alkaline activators for high performance concrete. Construction and Building Materials, 2012. 35: p. 1056-1062.

16. Fakhfakh, E., et al., Effects of sand addition on production of lightweight aggregates from Tunisian smectite-rich clayey rocks. Applied Clay Science, 2007. 35(3-4): p. 228-237.

17. Chiou, I.J., et al., Lightweight aggregate made from sewage sludge and incinerated ash. Waste Management, 2006. 26(12): p. 1453-1461.

18. Fragoulis, D., et al., Characterization of lightweight aggregates produced with clayey diatomite rocks originating from Greece. Materials Characterization, 2004. 53(2-4): p. 307-316.

19. González-Corrochano, B., J. Alonso-Azcárate, and M. Rodas, Characterization of lightweight aggregates manufactured from washing aggregate sludge and fly ash. Resources, Conservation and Recycling, 2009. 53(10): p. 571-581.

20. González-Corrochano, B., et al., Microstructure and mineralogy of lightweight aggregates manufactured from mining and industrial wastes. Construction and Building Materials, 2011. 25(8): p. 3591-3602.

21. Cheeseman, C.R., A. Makinde, and S. Bethanis, Properties of lightweight aggregate produced by rapid sintering of incinerator bottom ash. Resources, Conservation and Recycling, 2005. 43(2): p. 147-162.

22. Kourti, I. and C.R. Cheeseman, Properties and microstructure of lightweight aggregate produced from lignite coal fly ash and recycled glass. Resources, Conservation and Recycling, 2010. 54(11): p. 769-775.

23. Hiramatsu, Y. and Y. Oka, Determination of the tensile strength of rock by a compression test of an irregular test piece. International Journal of Rock Mechanics and Mining Sciences and, 1966. 3(2): p. 89-90.

24. CEN, EN 13055-1 Lightweight aggregates - Part 1: Lightweight aggregates for concrete, mortar and grout, 2002.

25. CEN, EN 1097-3: Tests for mechanical and physical properties of aggregates - Part 3: Determination of loose bulk density and voids, 1998.

26. Yang, C.-C. and R. Huang, Approximate strength of lightweight aggregate using micromechanics method. Advanced Cement Based Materials, 1998. 7(3-4): p. 133-138.

27. Harada, N., et al., A measurement of strength for artificial lightweight aggregate. Zairyo/Journal of the Society of Materials Science, Japan, 2000. 49(10): p. 1069-1074.

28. Li, Y., et al., Measurement and statistics of single pellet mechanical strength of differently shaped catalysts. Powder Technology, 2000. 113(1-2): p. 176-184.

29. Dexter, A.R. and B. Kroesbergen, Methodology for determination of tensile strength of soil aggregates. Journal of Agricultural Engineering Research, 1985. 31(2): p. 139-147.

30. McDowell, G.R., M.D. Bolton, and D. Robertson, The fractal crushing of granular materials. Journal of the Mechanics and Physics of Solids, 1996. 44(12): p. 2079-2102.

31. Jaeger, J.C., Failure of rocks under tensile conditions. International Journal of Rock Mechanics and Mining Sciences and, 1967. 4(2): p. 219-227.

32. Broch, E. and J.A. Franklin, The point-load strength test. International Journal of Rock Mechanics and Mining Sciences and, 1972. 9(6): p. 669-676.

33. Chung, J.H., J.K. Cochran, and K.J. Lee. Compressive mechanical behavior of hollow ceramic spheres. 1995.

34. Weibull, W., A Statistical Distribution Function of Wide Applicability. journal of applied mechanics, 1951. 18: p. 293-297.

35. Johnson, W., A.G. Mamalis, and Y. Mihara, The compression loading of solid spheres of plaster of Paris. International Journal of Mechanical Sciences, 1977. 19(6): p. 373-374,IN5-IN10,375-377.

36. Chau, K.T., et al., Fragmentation of brittle spheres under static and dynamic compressions: Experiments and analyses. Mechanics of Materials, 2000. 32(9): p. 543-554.

37. Warren, P.D., D.A. Hills, and D.N. Dai, Mechanics of Hertzian cracking. Tribology International, 1995. 28(6): p. 357-362.

38. Kschinka, B.A., et al., Strength of glass spheres in compression. Journal of the American Ceramic Society, 1986. 69(6): p. 467-472.

39. Tsoungui, O., et al., Size effects in single grain fragmentation. Granular Matter, 1999. 2(1): p. 19-27.

40. Shipway, P.H. and I.M. Hutchings, Fracture of brittle spheres under compression and impact loading. Philosophical Magazine A, 1993. 67(6): p. 1389-1404.

41. Shipway, P.H. and I.M. Hutchings, Attrition of brittle spheres by fracture under compression and impact loading. Powder Technology, 1993. 76(1): p. 23-30.

42. Dean, W.R., Sneddon, I.M., Parsons, H.W., Distribution of stress in a deccelerating elastic sphere. Selected Government Research Reports: Strength and Testing of Materials: Part II: Testing Methods and Test Results, 1952: p. 212-234.

43. McDowell, G.R., Statistics of soil particle strength. Geotechnique, 2001. 51(10): p. 90-897.

44. McDowell, G.R. and A. Amon, The application of weibull statistics to the fracture of soil particles. Soils and Foundations, 2000. 40(5): p. 133-141.

45. McDowell, G.R. and M.D. Bolton, On the micromechanics of crushable aggregates. Geotechnique, 1998. 48(5): p. 667-679.

46. Carlisle, K.B., et al., Structure and mechanical properties of micro and macro balloons: An overview of test techniques. Journal of Materials Science, 2006. 41(13): p. 3961-3972.

47. Carlisle, K.B., et al., Finite element modeling of the uniaxial compression behavior of carbon microballoons. Acta Materialia, 2007. 55(7): p. 2301-2318.

48. Richerson, D.W., Modern Ceramic Engineering third ed2006: Taylor and Francis group.

49. Griffith, A.A., The Phenomena of Rupture and Flow in Solids. Philosophical Transactions of the Royal Society of London. Series A,, 1920. Vol. 221: p. 163-198.

50. Brajer, X., et al., The role of surface and volume defects in the fracture of glass under quasi-static and dynamic loadings. Journal of Non-Crystalline Solids, 2003. 316(1): p. 42-53.

51. Vallet, D. and J.C. Charmet, Mechanical behaviour of brittle cement grains. Journal of Materials Science, 1995. 30(11): p. 2962-2967.

52. González-Corrochano, B., J. Alonso-Azcárate, and M. Rodas, Chemical partitioning in lightweight aggregates manufactured from washing aggregate sludge, fly ash and used motor oil. Journal of Environmental Management, 2012. 109: p. 43-53.

53. Miyoshi, T., et al., ALPORAS aluminum foam: Production process, properties, and applications. Advanced Engineering Materials, 2000. 2(4): p. 179-183.

54. Pernot, F., et al., Weibull parameters and the tensile strength of porous phosphate glass-ceramics. Journal of the American Ceramic Society, 1999. 82(3): p. 641-648.

55. Berryman, J.G., Random close packing of hard spheres and disks. Physical Review A, 1983. 27(2): p. 1053-1061.

Table captions:

Caption table 1: Equations reported in the literature to determine the stress occurring in a sphere or irregular shaped test piece under uniaxial compression. σ is equal to the stress, F the applied load, D the diameter of the sample and R the radius of the sample.

Caption table 2: Approximate mineralogical and chemical composition of the raw clay; Results are presented in wt.-%.

Caption table 3: Overview of the properties of samples produced in the rotary kiln (rot-) and in the laboratory (lab-); the numbers denote average diameter rounded in mm. Standard deviations are given in brackets.

Figure captions:

Caption Fig. 1: Illustration of LWA pellets produced in a pilot-scale rotary kiln. Diameters range from 1.8 mm (left) up to 12 mm (right).

Caption Fig. 2 Illustration of LWA pellets produced in a chamber furnace in the laboratory. Diameters range from 11 mm (left) up to 17 mm (right).

Caption Fig. 3: Illustration of one pellet of the series lab-16 (16 mm diameter) picturing the heterogeneity of the outer shell. The lower hemisphere exhibits a dense shell; the upper hemisphere exhibits a more porous shell.

Caption Fig. 4: Light microscope picture of the cross-section of a LWA pellet of 6 mm diameter produced in the rotary kiln showing the typical features of an LWA: A highly porous core surrounded by a relatively dense thin shell. The total porosity of the displayed pellet is approximately 82 %.

Caption Fig. 5: Particle density, $\rho_{particle}$, and porosity, *P*, of all samples produced in the rotary kiln and in the laboratory.

Caption Fig. 6: Calculated, theoretical expansion, *E*, of all samples.

Caption Fig. 7: Final sample diameter, *D*, as function of the solid diameter, *d*.

Caption Fig. 8: Failure load for all sample series; determined by the spc-test; error bars represent the standard deviation.

Caption Fig. 9: Relative standard deviation (%) of the failure load, F_{crit}, and the pellet diameter, *D*.

Caption Fig. 10: Typical load- displacement graph resulting from the compression of a single LWA pellet between rigid, parallel platens with a constant speed of displacement, 2 mm/min (spc-test).

Caption Fig. 11: Fracture patterns of LWA pellets after the spc-test. a) ruptured LWA pellet; b) typical fracture pattern of a pellet that splits into two hemispheres; c) typical fracture pattern of a pellet that splits into four evenly shaped pieces.

Caption Fig. 12: Crushing resistance, *C*, determined according to EN 13055-1 for the rot-4 to rot-9 samples; the insertion shows the loose bulk density for the same samples.

Caption Fig. 13: Failure load, F_{crit}, in dependency of the solid diameter, *d*, and the actual diameter, *D*, for all samples. The solid and dashed lines are the linear regressions of the series rot-2 to rot-6 and lab-11 to lab-14 respectively.

Caption Fig. 14: Failure load, F_{crit}, in dependency of the solid diameter, *d*, for all samples. The numbers denote the total porosity, *P (%)*. Eqs. 13-14 are represented by the solid lines.

Caption Fig. 15: Solid strength, σ_{crit}, as a function of the solid diameter, *d*, for all samples. The solid lines represent the trend of pellets with porosities less than 82 %. Pellets with porosities >82% show less strength than predicted by the solid lines.

Caption Fig. 16: Correlation between measured crushing resistance and calculated crushing resistance. The calculated crushing resistance 1 and 2 are based on Eqs. 16-17.